Anomalous Band Gap Behavior in Mixed Sn and Pb Perovskites Enables Broadening of Absorption Spectrum in Solar Cells

Feng Hao,[†,§] Constantinos C. Stoumpos,[†,§] Robert P. H. Chang,[‡] and Mercouri G. Kanatzidis*,[†]

[†]Department of Chemistry and [‡]Department of Materials Science and Engineering, and Argonne-Northwestern Solar Energy Research (ANSER) Center, Northwestern University, 2145 Sheridan Road, Evanston, Illinois 60208, United States

Ⓢ Supporting Information

ABSTRACT: Perovskite-based solar cells have recently been catapulted to the cutting edge of thin-film photovoltaic research and development because of their promise for high-power conversion efficiencies and ease of fabrication. Two types of generic perovskites compounds have been used in cell fabrication: either Pb- or Sn-based. Here, we describe the performance of perovskite solar cells based on alloyed perovskite solid solutions of methylammonium tin iodide and its lead analogue ($CH_3NH_3Sn_{1-x}Pb_xI_3$). We exploit the fact that, the energy band gaps of the mixed Pb/Sn compounds do not follow a linear trend (the Vegard's law) in between these two extremes of 1.55 and 1.35 eV, respectively, but have narrower bandgap (<1.3 eV), thus extending the light absorption into the near-infrared (~1,050 nm). A series of solution-processed solid-state photovoltaic devices using a mixture of organic spiro-OMeTAD/lithium bis(trifluoromethylsulfonyl)imide/pyridinium additives as hole transport layer were fabricated and studied as a function of Sn to Pb ratio. Our results show that $CH_3NH_3Sn_{0.5}Pb_{0.5}I_3$ has the broadest light absorption and highest short-circuit photocurrent density ~20 mA cm^{-2} (obtained under simulated full sunlight of 100 mW cm^{-2}).
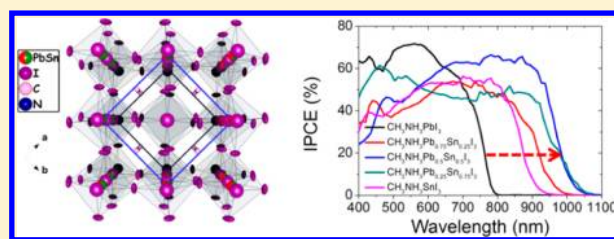
INTRODUCTION

In the push to meet the renewable energy needs of modern society,[1−4] it is essential to develop inexpensive and environmentally friendly energy conversion and storage systems. Photovoltaic research and development has been growing rapidly to make use of the world's most abundant and clean energy source, sunlight.[5−8] Historically, conventional photovoltaics have been expensive due to the complex fabrication procedures and high price of raw materials, and this has directly motivated a burgeoning field of research in solar technologies fabricated from fundamentally low-cost materials employing inexpensive fabrication methods.[9−13] Notably, a recent surge of organic−inorganic halide hybrid perovskites as light harvesters and hole transport materials has revolutionized the prospects of emerging photovoltaic technologies.[14−24]

The organic−inorganic hybrid perovskite compounds based on metal halides adopt the ABX_3 perovskite structure. This structure consists of a network of corner-sharing BX_6 octahedra, where the B atom is a metal cation (typically Sn^{2+} or Pb^{2+}) and X is a monovalent anion (typically F^-, Cl^-, Br^-, or I^-); the A cation is selected to balance the total charge, and it can be a Cs^+ or a small molecular species.[25−27] Recent implementation of $CH_3NH_3PbX_3$(X = Cl, Br, I) perovskite absorbers employing a cocktail containing 2,2′,7,7′-tetrakis(N,N-di-p-methoxyphenylamine)9,9′-spirobifluorene (spiro-OMeTAD)[28] as the organic hole conductor delivered power conversion efficiencies over 15%,[20,29] which has been boldly predicted as the "next big thing in photovoltaics".[30−33] A planar heterojunction photovoltaic device incorporating vapor-deposited perovskite ($CH_3NH_3PbI_{3-x}Cl_x$) as the absorbing layer showed overall power conversion efficiencies of over 15% with a high open-circuit voltage up to 1.07 V, further highlighting the industrial application potential in the near future.[19] Recent studies indicated the mixed-halide organic−inorganic hybrid perovskites displaying electron−hole diffusion lengths over 1 μm, which is consistent with our reports of very high carrier mobilities in these materials[34] and supports our expectations for highly efficient and cheap solar cells using thick absorption layers.[35,36]

One important strategy to further enhance the photovoltaic performance of perovskite solar cells lies in broadening the light absorption to the near-infrared spectrum, where the current $CH_3NH_3PbX_3$ perovskite shows a poor response over 780 nm due to its limited optical band gap of 1.55 eV.[17,19,20,29] An ideal light harvester should be panchromatic, that is, absorb all visible as well as some of the near-infrared light of the solar spectrum. A maximum theoretical efficiency in a single junction device is over 30%, achievable by harvesting the ultraviolet to near-infrared photons up to 1.1 eV.[37] However, synthesis of stable low-band gap perovskites for efficient light-to-electricity conversion is still a major challenge.[30−32] Meanwhile, finding ways to create lead-free perovskites without sacrificing device performance is especially critical since the well-known Pb toxicity hampers the practicality of such perovskite photovoltaics.[38]

Table 1. Lattice Parameters of the CH₃NH₃Sn₁₋ₓPbₓI₃ Solid Solution Prepared through the Solution Method and Compared with the Simulated Data (Cu Kα)

comp.	SGR	a (Å)	b (Å)	c (Å)	$\alpha = \beta = \gamma$ (°)	volume (Å³)
$CH_3NH_3SnI_3$_sim	P4mm	6.230 (1)	6.230(1)	6.231(1)	90	241.88(7)
$CH_3NH_3SnI_3$	P4mm	6.240(1)	6.240(1)	6.281(2)	90	244.60(5)
$CH_3NH_3Sn_{0.75}Pb_{0.25}I_3$	P4mm	6.283(1)	6.283(1)	6.314(2)	90	249.25(6)
$CH_3NH_3Sn_{0.50}Pb_{0.50}I_3$	P4mm	6.348(2)	6.348(2)	6.379(5)	90	257.08(19)
$CH_3NH_3Sn_{0.43}Pb_{0.57}I_3$_sim	I4cm	8.855(1)	8.855(1)	12.535(1)	90	982.95(13)
$CH_3NH_3Sn_{0.25}Pb_{0.75}I_3$	I4cm	8.930(1)	8.930(1)	12.599(8)	90	1004.68(61)
$CH_3NH_3PbI_3$	I4cm	8.929(1)	8.929(1)	12.688(8)	90	1011.50(60)
$CH_3NH_3PbI_3$_sim	I4cm	8.8494(13)	8.8494(13)	12.642(3)	90	990.02(4)

Our recent work on the hybrid metal iodide perovskites series showed (see Table 1) that solid solutions between the Sn and Pb perovskite compounds are readily accessible throughout the composition range spanning the optical band gap range between 1.1 and 1.7 eV, making them highly relevant as possible light absorbers in energy conversion or detector devices.[34] A recent study of Ogimi et al. reported a mixed bivalent metal, Sn−Pb perovskite which allowed tunability of the band gap of the perovskite absorber by varying the Sn:Pb ratio, indicating that Sn could be a potential choice of lead-free metal ion, especially for lower band gap solar cells.[39] However, this study reported that the neat $CH_3NH_3SnI_3$ perovskite does not exhibit significant photovoltaic properties and that a minimum content of Pb is needed to stabilize Sn in its 2⁺ state. Here, the alloyed perovskites of methylammonium tin iodide ($CH_3NH_3SnI_3$) and its lead analogue ($CH_3NH_3PbI_3$) are implemented as novel panchromatic light absorbing material to fabricate solution-processed solid-state photovoltaic devices in conjunction with an organic hole transport layer. Notably, incident photon-to-electron conversion efficiency (IPCE) response spanning the whole visible and infrared spectrum (up to 1050 nm) has been realized for the first time with the solid solution $CH_3NH_3Pb_{1-x}Sn_xI_3$, which is currently the broadest absorption range reported for high-performing perovskite-based devices.[40−42] A promising short-circuit photocurrent density of 20.64 mA cm⁻² is obtained with mesoporous TiO₂ electrode and spiro-OMeTAD hole transport layer under simulated full sunlight of 100 mW cm⁻². Higher photocurrent density would be expected by further device optimization to minimize the charge recombination and maximize the light harvesting capacity.

■ RESULTS AND DISCUSSION

$CH_3NH_3Sn_{1-x}Pb_xI_3$ compounds were prepared by mixing stoichiometric amounts of CH_3NH_3I and MX_2, (M = Sn, Pb) in an aqueous HI/H_3PO_2 (4:1) solvent mixture to afford a bright yellow solution at ∼100 °C. Slow cooling of the solution to room temperature affords highly crystalline $CH_3NH_3Sn_{1-x}Pb_xI_3$ with only small deviations on x with respect to the nominal composition. The $CH_3NH_3Sn_{1-x}Pb_xI_3$ solid solution discussed in this work adopts the perovskite structure type consisting of corner-sharing $[Sn_{1-x}Pb_xI_6]^{-4}$ octahedra in which the metal site is randomly occupied by either Sn or Pb atoms (see Table 1). The two end members, namely $CH_3NH_3SnI_3$ and $CH_3NH_3PbI_3$, crystallize in the pseudocubic P4mm (α-phase) and tetragonal I4cm (β-phase) space groups, respectively, at ambient conditions (Figure 1a,c). At elevated temperatures (∼330 K), $CH_3NH_3PbI_3$ undergoes a reversible structural phase transition to the P4mm space group becoming isostructural to its Sn analogue. The same structural
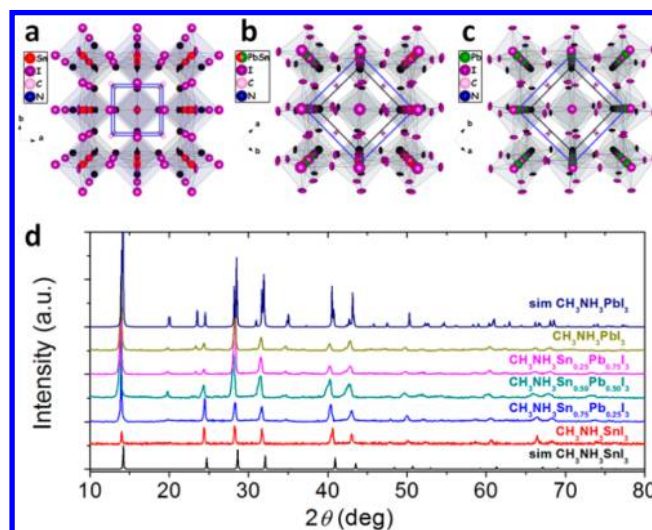
Figure 1. Crystal structure and X-ray diffraction pattern of the $CH_3NH_3Sn_{1-x}Pb_xI_3$ solid solutions. Crystal structure (a, b, and c) and X-ray diffraction pattern (d) of the $CH_3NH_3Sn_{1-x}Pb_xI_3$ solid solutions. Simulated X-ray diffraction patterns of the two end compositions of $CH_3NH_3PbI_3$ and $CH_3NH_3SnI_3$ are also shown in (d).

transition can be also realized in the $CH_3NH_3Sn_{1-x}Pb_xI_3$ solid solution for an $x \sim 0.5$ value at room temperature (Figure 1b). It is obvious from the X-ray diffraction patterns in Figure 1d that the two peaks within the range between 22°−25° 2θ ($x <$ 0.5), which could be indexed to (211) and (202) planes in the tetragonal I4cm space group, can gradually merge to a single peak corresponding to the (113) plane in the P4mm space group when x becomes >0.5 due to the higher symmetry of P4mm.[34] Such a transition involves a distortion of the relative positions of the octahedra about the 4-fold crystallographic axis (c-axis). Thus, in the ideal case of $CH_3NH_3SnI_3$, the tilting angle between the $[SnI_6]^{-4}$ octahedra is 177.43(1)° slightly deviating from the ideal straight angle. In $CH_3NH_3PbI_3$, the tilting angle becomes larger at 163.55(1)° significantly distorting the $(PbI_3)^-$ framework, thereby reducing the symmetry of the unit cell. For comparison, in the intermediate $CH_3NH_3Sn_{0.43}Pb_{0.57}I_3$ composition, which adopts the tetragonal I4cm structure,[34] the corresponding angle is 169.43(1)°. It has to be noted that the deviation from the ideal cubic (Pm-3m) structure arises from orientational ordering of the $CH_3NH_3^+$ cation along the crystallographic c-axis. The crystallographic P4mm and I4cm unit cells are related to one another by a $a\sqrt{2} \times b\sqrt{2} \times 2c$ relation resulting in a 4-fold increase in the cell's volume. This is a distinctive feature of the $CH_3NH_3^+$-based perovskites over $Cs(Sn/Pb)I_3$ (P4/mbm)[43] and HC-$(NH_2)_2(Sn/Pb)I_3$ (Amm2)[34] ones where the $a\sqrt{2} \times b\sqrt{2} \times c$

relation applies leading to doubling of the unit cell. The difference between the two structural types arises from the tilting of the octahedra, which in the case of, for example, $CH_3NH_3PbI_3$ occurs in opposite sense along the (pseudo)-tetragonal axis (out-of-plane tilting) compared to β-$CsSnI_3$ and α-$HC(NH_2)_2SnI_3$ (in-phase tilting).

These structural qualities of the perovskites are reflected in their charge-transport properties since the orbital overlap, and therefore the electrical conductivity become optimal for the least distorted Sn/Pb–I–Sn/Pb angles. In $CH_3NH_3SnI_3$, the Sn–I–Sn bond angle deviates only slightly from linearity, and therefore the compound displays the highest conductivity among the $CH_3NH_3Sn_{1-x}Pb_xI_3$ compositions, whereas $CH_3NH_3PbI_3$ which has the largest Pb–I–Pb tilting angle is the least conductive (Figure 2). Since the compounds are
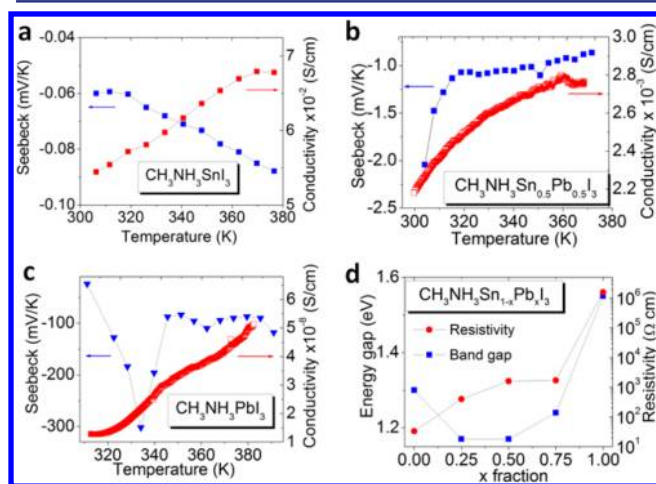

Figure 2. Transport and optoelectronic measurements of the $CH_3NH_3Sn_{1-x}Pb_xI_3$ solid solutions. Conductivities and Seebeck coefficients (a, b, and c) as a function of temperature for the $CH_3NH_3Sn_{1-x}Pb_xI_3$ solid solutions prepared from the solution method. Dependence of resistivity and optical band gap of the $CH_3NH_3Sn_{1-x}Pb_xI_3$ on the x fraction is summarized in (d).

prepared by an identical method and therefore have a comparable, close to intrinsic carrier concentration, the trend can likely be extended to the carrier mobilities. Interestingly, the mixed compositions do not follow a linear trend in resistivity as a function of x as it would have been expected in the case of a genuine solid solution (i.e., Vegard's law). The

non-Vegard's law behavior is additionally verified by the irregular evolution of the lattice parameters as a function of increased Pb content (Figure S1). Instead, the resistivity properties of the Sn end-member appear to dominate over the Pb one up to $x = 0.75$ (Figure 2).

All compositions behave as semiconductors as evidenced by the increase in conductivity with increasing temperature which is also consistent with the optically determined energy gap in the range of 1.15–1.55 eV. In addition, Seebeck coefficient measurements suggest that all compositions in the solid solution behave as n-type semiconductors with the Seebeck coefficient decreasing dramatically as the x-value (i.e., Pb content) increases. The corresponding carrier concentrations for the compounds used in this work are in the range of ~1.1 × 10^{14} cm^{-3} for $CH_3NH_3SnI_3$ and ~4.8 × 10^{11} cm^{-3} for $CH_3NH_3PbI_3$, with the solid solutions lying in between. This decrease is proportional to the relative decrease in carrier concentration dictated by the band gap. An analogous trend is observed for state-of-the-art semiconductors with similar band gaps, e.g., Si (E_g = 1.12 eV) has an intrinsic carrier concentration of 1 × 10^{10} cm^{-3}, whereas GaAs (E_g = 1.42 eV) has an intrinsic carrier concentration of 2.1 × 10^6 cm^{-3}.[44]

The optical band gaps (E_g) of the $CH_3NH_3Sn_{1-x}Pb_xI_3$ solid solutions were determined from diffuse reflectance measurements. Figure 3a shows the transformed Kubelka–Munk UV–vis near-IR absorption spectra for the synthesized $CH_3NH_3Sn_{1-x}Pb_xI_3$ serial compounds. The optical absorption coefficient (α/S) is calculated using reflectance data according to the Kubelka–Munk equation,[45] $\alpha/S = (1 - R)^2/2R$, where R is the percentage of reflected light, and α and S are the absorption and scattering coefficients, respectively. Notably, by stoichiometrically mixing the divalent metal iodides of Sn and Pb with methylammonium iodide, we can easily synthesize the $CH_3NH_3Sn_{1-x}Pb_xI_3$ solid solutions with a tunable bandgap tunable between 1.17 and 1.55 eV. The intermediate compounds with $x = 0.25$ and 0.5 show the smallest bandgaps of 1.17 eV. It is important to note that the optimal bandgap for a single-junction solar cell is between 1.1 and 1.4 eV, currently beyond the range of most investigated methylammonium lead trihalide systems.[46] The $CH_3NH_3Sn_{1-x}Pb_xI_3$ series is therefore promising for more efficient photovoltaic devices for both the single junction and also tandem architecture device where the optimum bandgap for a bottom cell lies in around 1 eV.[46]

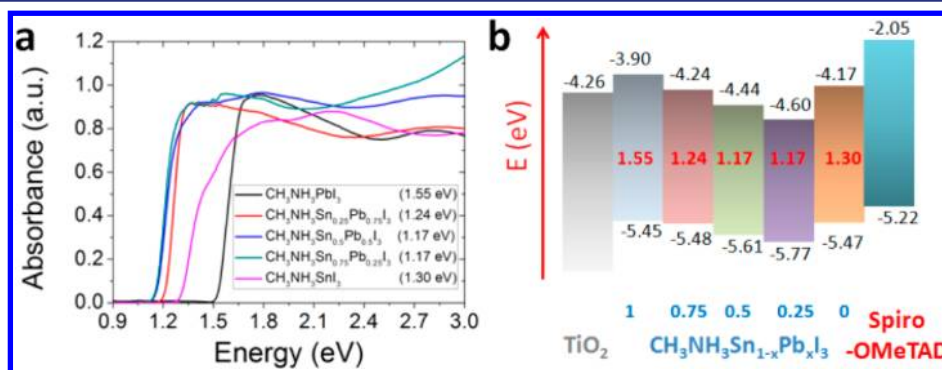The valence band energies (E_{VB}) of the $CH_3NH_3Sn_{1-x}Pb_xI_3$ compounds were further probed by ultraviolet photoelectron

Figure 3. Absorption spectra and schematic energy level diagram of the $CH_3NH_3Sn_{1-x}Pb_xI_3$ solid solution perovskites. (a) Electronic absorption spectra and (b) schematic energy level diagram of the $CH_3NH_3Sn_{1-x}Pb_xI_3$ solid solution perovskites. The valence band maxima (E_{CB}) of the hybrid methylammonium tin/lead triiodides were extracted from UPS measurements under high vacuum.
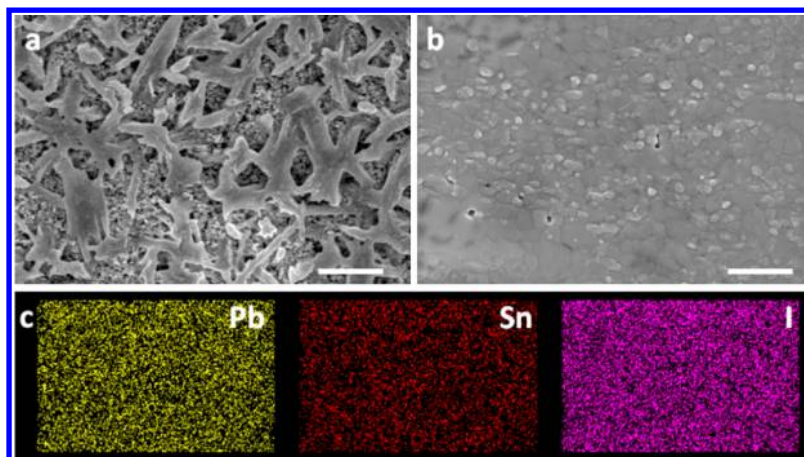
Figure 4. Representative SEM images of the (a) $CH_3NH_3PbI_3$ and (b) $CH_3NH_3Sn_{0.5}Pb_{0.5}I_3$ films on top of the mesoporous TiO_2 electrodes. The scale bars represent 1 μm. (c) EDS elemental mapping of Pb, Sn and I in film (b).
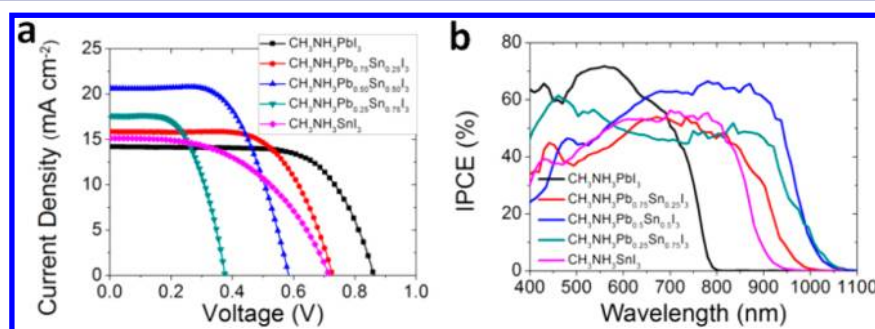

Figure 5. Photovoltaic performance of device with $CH_3NH_3Sn_{1-x}Pb_xI_3$ perovskites. (a) Photocurrent density–voltage (J–V) characteristics and (b) corresponding IPCE spectra of the devices based on $CH_3NH_3Sn_{1-x}Pb_xI_3$ (x = 0, 0.25, 0.5, 0.75, and 1) perovskites.

Table 2. Photovoltaic Performance Parameters of the $CH_3NH_3Sn_{1-x}Pb_xI_3$ (x = 0, 0.25, 0.5, 0.75, 1) Perovskite Solar Cells under Simulated Full Sunlight of 100 mW cm^{-2}

methylammonium perovskite	J_{sc} (mA cm^{-2})	J_{int} (mA cm^{-2})	V_{oc} (V)	FF (%)	PCE (%)
$CH_3NH_3SnI_3$	15.18	14.96	0.716	50.07	5.44
$CH_3NH_3Sn_{0.75}Pb_{0.25}I_3$	17.55	17.82	0.376	56.64	3.74
$CH_3NH_3Sn_{0.5}Pb_{0.5}I_3$	20.64	20.33	0.584	60.32	7.27
$CH_3NH_3Sn_{0.25}Pb_{0.75}I_3$	15.82	15.70	0.728	64.01	7.37
$CH_3NH_3PbI_3$	14.16	14.30	0.863	68.03	8.31

spectroscopy (UPS). As demonstrated in the schematic energy level diagram of Figures 3b and S2, the E_{VB} is estimated to decrease from −5.45 eV below vacuum level for $CH_3NH_3PbI_3$ to −5.77 eV when decreasing the x fraction from 1 to 0.25. However, the E_{VB} for the tin-end compound $CH_3NH_3SnI_3$ is found to be around −5.47 eV, which is comparable to that of the pure lead compound $CH_3NH_3PbI_3$. From the observed optical band gaps, the conduction band energy (E_{CB}) of $CH_3NH_3Sn_{1-x}Pb_xI_3$ compounds is also shown in the diagram of Figure 3b.

Figure 4 shows two representative SEM images of $CH_3NH_3PbI_3$ and $CH_3NH_3Sn_{0.5}Pb_{0.5}I_3$ films on mesoporous TiO_2 electrodes, respectively. The $CH_3NH_3PbI_3$ film is composed of interconnected nanoscale domains with sizes ranging from 200 to 500 nm with decent film coverage. However, the $CH_3NH_3Sn_{0.5}Pb_{0.5}I_3$ film displays far superior film quality and coverage. This markedly increased film coverage ensures connectivity between grains, which is crucial to mitigate short-circuiting, charge leaking, and large series resistance. Compared to the $CH_3NH_3PbI_3$ film, contrast

features apparent in the hybrid $CH_3NH_3Pb_{0.5}Sn_{0.5}I_3$ film suggest the formation of smaller crystallite domains implying a more efficient film formation via favorable crystal growth of the mixed-metal perovskite.[47,48] Figure 4c shows elemental maps of Pb, Sn, and I in $CH_3NH_3Sn_{0.5}Pb_{0.5}I_3$ film obtained via SEM energy-dispersive X-ray spectroscopy (EDS). It is apparent that Sn and Pb are homogeneously distributed throughout the film with no evident phase separation. The quantitative EDS analysis shows a Pb:Sn atomic ratio around 54:46 in the $CH_3NH_3Sn_{0.5}Pb_{0.5}I_3$ film, which is quite close to the nominal 50:50 ratio given by stoichiometry of the precursor solutions. Similar quantitative results were also obtained from the X-ray photoelectron spectroscopy (XPS) analysis as shown in Figure S3.

Solid devices were constructed with the $CH_3NH_3Sn_{1-x}Pb_xI_3$ perovskites as light harvesters and 2,2′,7,7′-tetrakis(N,N-di-p-methoxyphenylamine)-9,9′-spirobifluorene (spiro-MeOTAD) with lithium bis(trifluoromethylsulfonyl)imide and pyridinium additives as hole-transporting materials (HTM). Figure 5a,b presents the representative photocurrent density–voltage (J–

V) characteristics and incident-photon-conversion-efficiency (IPCE) spectra for these devices. The photovoltaic parameters are selectively summarized in Table 2. The solid-state device based on the lead-free $CH_3NH_3SnI_3$ perovskite shows a decent short-circuit photocurrent density (J_{sc}) of 15.18 mA cm^{-2}, an open-circuit voltage (V_{oc}) of 0.716 V and a fair fill factor (FF) of 50.07% under AM1.5G solar illumination, corresponding to a power conversion efficiency (PCE) of 5.44%. It is important to note that this is an example of a lead-free perovskite solar cell with a decent conversion efficiency. The obtained current density is lower compared to the reported high-efficiency $CH_3NH_3PbI_3$ perovskite solar cells,[18−23,29] which might be related to the poor perovskite film quality and low coverage on the mesoporous TiO_2 electrode. However, the incident photon-to-electron conversion efficiency (IPCE) of the $CH_3NH_3SnI_3$ device covers the entire visible spectrum and reaches a broad absorption maximum over 50% from 500 to 850 nm accompanied by a notable absorption onset up to 950 nm (Figure 5b), which is in good agreement with the optical band gap of 1.3 eV. Integrating the overlap of the IPCE spectrum with the AM1.5G solar photon flux yields a current density of 14.96 mA cm^{-2}, which is in excellent agreement with the measured photocurrent density. This confirms that any mismatch between the simulated sunlight and the AM1.5G standard is negligibly small. Notably, the obtained V_{oc} is significantly higher than the reported value by Ogimi et al., indicating that Sn halide perovskite itself did not show photovoltaic properties.[39] The low photovoltage for the Sn perovskite devices observed in the literature report can be mainly ascribed to the obvious observation of the Sn^{2+} oxidation in the Sn perovskites, as it is evident from the extra Bragg peaks at approximately 15° and 30° in the X-ray powder diffraction profiles. The extra peaks can be indexed to the Sn^{4+} $(CH_3NH_3)_2SnI_6$ compound.[34] This can occur either from self-doping of the Sn perovskite[49,50] or from exposure-induced oxidation during the device preparation procedures. Furthermore, we note that the complex soup-like combination of additives commonly used with spiro-OMeTAD, lithium bis(trifluoromethylsulfonyl)imide salt, and 4-*tert*-butylpyridine are too reactive and not compatible with the Sn perovskites, thus making these devices nonfunctional or unstable, even in the inert atmosphere condition. Similar phenomenon has also been noticed in a recent study on the pure Sn perovskite.[51]

It is striking that even a slight Pb incorporation in the pure tin perovskite directly red shifts the absorption onset to the near-infrared spectrum, as indicated from the IPCE spectra in Figure 5b. Consistent with the band gap reduction, the onset of the IPCE spectra shift from 950 nm for the pure tin perovskite to almost 1050 nm for the $CH_3NH_3Sn_{0.75}Pb_{0.25}I_3$ and $CH_3NH_3Sn_{0.5}Pb_{0.5}I_3$ perovskites (corresponds to a E_g of 1.17 eV). Further increasing the Pb content to 75% enable an attenuated onset around 1000 nm, which agrees well with a E_g of 1.23 eV. All devices showed significantly extended solar absorption range when compared to the most investigated pure lead perovskite $CH_3NH_3PbI_3$ device with an IPCE onset of 800 nm, in accordance with the reported $CH_3NH_3PbI_3$ perovskite solar cells.[18−23,29] Integrating the overlap of these IPCE spectra with the AM1.5G solar photon flux yield similar current density (J_{int}) with the measured photocurrent density (J_{sc}), as tabulated in Table 2.

This is the first report of IPCE responses spanning the whole visible and infrared spectrum (up to 1050 nm) with the solid solution $CH_3NH_3Sn_{1−x}Pb_xI_3$ perovskites, which is currently the broadest absorption range reported for high-performing perovskite-based devices.[40−42] Interestingly, the V_{oc} decreased from 0.863 to 0.376 V when switching from the pure lead perovskite to the solid solution of $CH_3NH_3Sn_{0.75}Pb_{0.25}I_3$. The deduction of V_{oc} can be attributed to the lower conduction band edge (E_{CB}) with decreasing Pb content in $CH_3NH_3Sn_{1−x}Pb_xI_3$ solid solution as evidently demonstrated in the energy diagram of Figure 3b.[52] Meanwhile, the obtained FF is significantly lower than the reported values for high-efficient perovskite solar cells,[19,20,29] which might be related to associated p-type doping which can occur via Sn^{2+} oxidation during the device fabrication process.[49] Further FF enhancements would also be expected from more efficient interfacial engineering to inhibit the back electron recombination.

■ CONCLUSION

We have demonstrated that by using the alloyed perovskite solid solutions of methylammonium lead iodide ($CH_3NH_3PbI_3$) and its tin analogue ($CH_3NH_3SnI_3$) panchromatic light harvesters in solution-processed solid-state photovoltaic devices can be achieved with extended light absorption range into the near IR (1.1 eV or 1050 nm). This is possible because of the anomalous band gap change in the $CH_3NH_3Pb_{1−x}Sn_xI_3$ compositions. As a function of x a lower band gap can be obtained than either of the two end members, and thus we can extended the absorption range down to 1.1 eV. These results have been confirmed by optical measurements of the materials as well as data taken from IPCE responses of the respective devices. For example, an optimal short-circuit photocurrent density over 20 mA cm^{-2} has been obtained for the mixed alloy $CH_3NH_3Sn_{0.5}Pb_{0.5}I_3$ obtained under simulated full sunlight of 100 mW cm^{-2}. The anomalous trend in band gap of compositions lying between $CH_3NH_3PbI_3$ and $CH_3NH_3SnI_3$ end-members may have the same origin as the similar anomalous trend observed in $Pb_{1−x}Sn_xTe$. In these chalcogenide systems a band inversion occurs with varying x which is associated with a systematic change in the atomic orbital composition of the conduction and valence bands. This is because the conduction band minimum in SnTe has a similar orbital composition as the valence band maximum in PbTe and vice versa.[53] This causes the energy gap to follow an anomalous trend rather than the expected Vegard's law trend. A deeper understanding of this unique effect, which is responsible for being able to significantly extend the solar absorption spectrum of the perovskite based systems, will require careful electronic band structure calculations.

■ ASSOCIATED CONTENT

Ⓢ Supporting Information

Detailed experimental procedures and Figures S1−S3. This material is available free of charge via the Internet at http://pubs.acs.org.

■ AUTHOR INFORMATION

Corresponding Author

m-kanatzidis@northwestern.edu

Author Contributions

§These authors contributed equally.

Notes

The authors declare no competing financial interest.

ACKNOWLEDGMENTS

REFERENCES

(1) Lewis, N. S.; Nocera, D. G. *Proc. Natl. Acad. Sci. U. S. A.* **2006**, *103*, 15729.

(2) Hoffert, M. I.; Caldeira, K.; Benford, G.; Criswell, D. R.; Green, C.; Herzog, H.; Jain, A. K.; Kheshgi, H. S.; Lackner, K. S.; Lewis, J. S.; Lightfoot, H. D.; Manheimer, W.; Mankins, J. C.; Mauel, M. E.; Perkins, L. J.; Schlesinger, M. E.; Volk, T.; Wigley, T. M. L. *Science* **2002**, *298*, 981.

(3) Nozik, A. J. *Annu. Rev. Phys. Chem.* **1978**, *29*, 189.

(4) Gust, D.; Moore, T. A.; Moore, A. L. *Acc. Chem. Res.* **2001**, *34*, 40.

(5) Kamat, P. V.; Tvrdy, K.; Baker, D. R.; Radich, J. G. *Chem. Rev.* **2010**, *110*, 6664.

(6) Kippelen, B.; Bredas, J. L. *Energy Environ. Sci.* **2009**, *2*, 251.

(7) Graetzel, M.; Janssen, R. A. J.; Mitzi, D. B.; Sargent, E. H. *Nature* **2012**, *488*, 304.

(8) Shah, A.; Torres, P.; Tscharner, R.; Wyrsch, N.; Keppner, H. *Science* **1999**, *285*, 692.

(9) Trindade, T.; O'Brien, P.; Pickett, N. L. *Chem. Mater.* **2001**, *13*, 3843.

(10) Winkler, M. T.; Wang, W.; Gunawan, O.; Hovel, H. J.; Todorov, T. K.; Mitzi, D. B. *Energy Environ. Sci.* **2014**, *7*, 1029.

(11) Coughlin, J. E.; Henson, Z. B.; Welch, G. C.; Bazan, G. C. *Acc. Chem. Res.* **2014**, *47*, 257.

(12) Kramer, I. J.; Sargent, E. H. *Chem. Rev.* **2014**, *114*, 863.

(13) Li, G.; Zhu, R.; Yang, Y. *Nat. Photonics* **2012**, *6*, 153.

(14) Chung, I.; Lee, B.; He, J. Q.; Chang, R. P. H.; Kanatzidis, M. G. *Nature* **2012**, *485*, 486.

(15) Kojima, A.; Teshima, K.; Shirai, Y.; Miyasaka, T. *J. Am. Chem. Soc.* **2009**, *131*, 6050.

(16) Etgar, L.; Gao, P.; Xue, Z. S.; Peng, Q.; Chandiran, A. K.; Liu, B.; Nazeeruddin, M. K.; Grätzel, M. *J. Am. Chem. Soc.* **2012**, *134*, 17396.

(17) Kim, H. S.; Lee, C. R.; Im, J. H.; Lee, K. B.; Moehl, T.; Marchioro, A.; Moon, S. J.; Humphry-Baker, R.; Yum, J. H.; Moser, J. E.; Grätzel, M.; Park, N. G. *Sci. Rep.* **2012**, *2*, 591.

(18) Heo, J. H.; Im, S. H.; Noh, J. H.; Mandal, T. N.; Lim, C. S.; Chang, J. A.; Lee, Y. H.; Kim, H. J.; Sarkar, A.; Nazeeruddin, M. K.; Grätzel, M.; Seok, S. I. *Nat. Photonics* **2013**, *7*, 487.

(19) Liu, M. Z.; Johnston, M. B.; Snaith, H. J. *Nature* **2013**, *501*, 395.

(20) Burschka, J.; Pellet, N.; Moon, S. J.; Humphry-Baker, R.; Gao, P.; Nazeeruddin, M. K.; Grätzel, M. *Nature* **2013**, *499*, 316.

(21) Kim, H. S.; Lee, J. W.; Yantara, N.; Boix, P. P.; Kulkarni, S. A.; Mhaisalkar, S.; Grätzel, M.; Park, N. G. *Nano Lett.* **2013**, *13*, 2412.

(22) Abrusci, A.; Stranks, S. D.; Docampo, P.; Yip, H. L.; Jen, A. K. Y.; Snaith, H. J. *Nano Lett.* **2013**, *13*, 3124.

(23) Ball, J. M.; Lee, M. M.; Hey, A.; Snaith, H. J. *Energy Environ. Sci.* **2013**, *6*, 1739.

(24) Abu Laban, W.; Etgar, L. *Energy Environ. Sci.* **2013**, *6*, 3249.

(25) Borriello, I.; Cantele, G.; Ninno, D. *Phys. Rev. B* **2008**, *77*, 235214.

(26) Mitzi, D. B. *Prog. Inorg. Chem.* **1999**, *48*, 1.

(27) Kagan, C. R.; Mitzi, D. B.; Dimitrakopoulos, C. D. *Science* **1999**, *286*, 945.

(28) Bach, U.; Lupo, D.; Comte, P.; Moser, J. E.; Weissortel, F.; Salbeck, J.; Spreitzer, H.; Grätzel, M. *Nature* **1998**, *395*, 583.

(29) Lee, M. M.; Teuscher, J.; Miyasaka, T.; Murakami, T. N.; Snaith, H. J. *Science* **2012**, *338*, 643.

(30) Snaith, H. J. *J. Phys. Chem. Lett.* **2013**, *4*, 3623.

(31) Park, N. G. *J. Phys. Chem. Lett.* **2013**, *4*, 2423.

(32) Hodes, G. *Science* **2013**, *342*, 317.

(33) Bisquert, J. *J. Phys. Chem. Lett.* **2013**, *4*, 2597.

(34) Stoumpos, C. C.; Malliakas, C. D.; Kanatzidis, M. G. *Inorg. Chem.* **2013**, *52*, 9019.

(35) Xing, G. C.; Mathews, N.; Sun, S. Y.; Lim, S. S.; Lam, Y. M.; Grätzel, M.; Mhaisalkar, S.; Sum, T. C. *Science* **2013**, *342*, 344.

(36) Stranks, S. D.; Eperon, G. E.; Grancini, G.; Menelaou, C.; Alcocer, M. J. P.; Leijtens, T.; Herz, L. M.; Petrozza, A.; Snaith, H. J. *Science* **2013**, *342*, 341.

(37) Shockley, W.; Queisser, H. J. *J. Appl. Phys.* **1961**, *32*, 510.

(38) Loi, M. A.; Hummelen, J. C. *Nat. Mater.* **2013**, *12*, 1087.

(39) Ogomi, Y.; Morita, A.; Tsukamoto, S.; Saitho, T.; Fujikawa, N.; Shen, Q.; Toyoda, T.; Yoshino, K.; Pandey, S. S.; Ma, T.; Hayase, S. *J. Phys. Chem. Lett.* **2014**, *5*, 1004.

(40) Noh, J. H.; Im, S. H.; Heo, J. H.; Mandal, T. N.; Seok, S. I. *Nano Lett.* **2013**, *13*, 1764.

(41) Koh, T. M.; Fu, K.; Fang, Y.; Chen, S.; Sum, T. C.; Mathews, N.; Mhaisalkar, S. G.; Boix, P. P.; Baikie, T. *J. Phys. Chem. C* **2013**, ASAP, DOI: 10.1021/jp411112k.

(42) Eperon, G. E.; Stranks, S. D.; Menelaou, C.; Johnston, M. B.; Herz, L. M.; Snaith, H. J. *Energy Environ. Sci.* **2014**, *7*, 982.

(43) Chung, I.; Song, J. H.; Im, J.; Androulakis, J.; Malliakas, C. D.; Li, H.; Freeman, A. J.; Kenney, J. T.; Kanatzidis, M. G. *J. Am. Chem. Soc.* **2012**, *134*, 8579.

(44) *Handbook Series on Semiconductor Parameters*Levinstein, M., Rumyantsev, S., Shur, M., Eds.; World Scientific: London, 1999; Vol. 1,2.

(45) Gate, L. F. *Appl. Opt.* **1974**, *13*, 236.

(46) Meillaud, F.; Shah, A.; Droz, C.; Vallat-Sauvain, E.; Miazza, C. *Sol. Energy Mater. Sol. C* **2006**, *90*, 2952.

(47) Mitzi, D. B. *Chem. Mater.* **2001**, *13*, 3283.

(48) Liang, K. N.; Mitzi, D. B.; Prikas, M. T. *Chem. Mater.* **1998**, *10*, 403.

(49) Takahashi, Y.; Obara, R.; Lin, Z. Z.; Takahashi, Y.; Naito, T.; Inabe, T.; Ishibashi, S.; Terakura, K. *Dalton. Trans.* **2011**, *40*, 5563.

(50) Takahashi, Y.; Hasegawa, H.; Takahashi, Y.; Inabe, T. *J. Solid State Chem.* **2013**, *205*, 39.

(51) Noel, N. K.; Stranks, S. D.; Abate, A.; Wehrenfennig, C.; Guarnera, S.; Haghighirad, A.; Sadhanala, A.; Eperon, G. E.; Pathak, S. K.; Johnston, M. B.; petrozza, a.; Herz, L.; Snaith, H. *Energy Environ. Sci.* **2014**, DOI: 10.1039/C4EE01076K.

(52) Kim, H. S.; Mora-Sero, I.; Gonzalez-Pedro, V.; Fabregat-Santiago, F.; Juarez-Perez, E. J.; Park, N. G.; Bisquert, J. *Nat. Commun.* **2013**, *4*, 2242.

(53) Gao, X.; Daw, M. S. *Phys. Rev. B* **2008**, *77*, 033103.